Astronomy & Astrophysics manuscript no. output
May 16, 2023

Modulation depth of the gyrosynchotron emission as identifier of fundamental sausage modes

M. Cécere[1,2], A. Costa[1], and T. Van Doorsselaere[3]

[1] Instituto de Astronomía Teórica y Experimental, CONICET-UNC, Córdoba, Argentina.
[2] Observatorio Astronómico de Córdoba, UNC, Córdoba, Argentina.
[3] Centre for mathematical Plasma Astrophysics, Department of Mathematics, KU Leuven, Celestijnenlaan 200B bus 2400, B-3000, Leuven, Belgium.

ABSTRACT

Aims. We study the intensity, the modulation depth and the mean modulation depth of the gyrosynchotron (GS) radiation as a function of the frequency and the LOS in fast sausage modes.
Methods. By solving the 2.5D MHD ideal equations of a straight coronal loop considering the chromosphere and with typical flaring plasma parameters we analyse the wavelet transform of the density and the gyrosynchotron emission for different radio frequencies and different spatial resolutions, given impulsive and general perturbations with energies in the microflare range.
Results. A wavelet analysis performed over the GS radiation emission showed that a fast fundamental sausage mode of ~ 7 s with a first harmonic mode of 3 s developed, for all the initial energy perturbations used. For both the high spatial resolution (central pixel integration) and the low spatial resolution (entire loop integration), the larger the radio frequency, the larger the modulation depth. However, high and low resolution integrations differ in that, the larger the LOS angle with respect to the loop axis, results in a larger and smaller modulation depth, respectively.
Conclusions. Fast MHD modes triggered by instantaneous energy depositions of the order of a microflare energy are able to reproduce deep intensity modulation depths in radio emission as observed in solar events. As the trends of the GS emission obtained by Reznikova, Antolin, and Van Doorsselaere (2014), for a linear and forced oscillation, remain present when analysing a more general context, considering the chromosphere and where the sausage mode is triggered by a impulsive, nonlinear perturbation, it seems that the behaviour found can be used as observational identifiers of the presence of sausage modes with respect to other QPP features. It can be inferred from this that finite-amplitude sausage modes have the potential to generate the observed deep modulation depths.

Key words. Sun: oscillations; Sun: flares; Magnetohydrodynamics (MHD)

1. Introduction

Solar flares and stellar flares of M red dwarfs and solar-type active stars, which are still needed to last from several seconds to several hours, are the highest-energy processes of their atmospheres, capable of releasing a large amount of energy (Zimovets et al. 2021; Kupriyanova et al. 2020). The stellar flare energies are comparable or often considerably higher than the most powerful solar flare detected (Carrington 1859) with a total energy of $\sim 10^{32}$ erg. The so-called superflares are flares with a total energy of over 10^{33} erg, however detected in only ~ 0.1 of all the observed stars (Kolotkov et al. 2021). The study of stellar flares and superflares has become an important issue to investigate whether the Sun is capable of producing a damaging solar superflare.

In most of solar and stellar flares, quasi-periodic pulsations (QPP) were detected in all spectral bands, from low-frequency radio waves to high gamma-ray energies (for a review see e.g. Kupriyanova et al. (2020) and reference therein). The observed QPP periods vary from fractions of a second to tens of minutes and their duration is not longer than a few tens of oscillations (Nakariakov et al. 2019).

Several empirical similarities between stellar and solar QPPs in flares (Cho et al. 2016) strongly suggest that a common underlying physical mechanism could explain the phenomenon. Thus, these transient oscillations seem to be unique seismological tools to give account of non-spatially-resolved plasma conditions and processes in stars.

While the physical mechanisms responsible for producing this omnipresent behaviour are still not fully understood, three main mechanisms were proposed. The QPP signal could be produced by repetitive magnetic reconnections induced periodically by an MHD oscillation, the reconnection process itself could be repetitive and periodically triggered internally in a spontaneous wave (self-oscillations) or QPP signals would be the emission of the local plasma modulated by MHD oscillations (McLaughlin et al. 2018).

Due to the similarity between QPP periods in most of solar and stellar flares with respect to typical coronal MHD fast wave periods, we here investigate the emission properties of fast sausage modes as producers of QPP signals.

Sausage modes manifest observationally as quasi-periodic pulsation patterns. They are produced by collective plasma perturbations in relatively thick and short magnetic structures observed in flaring regions of low β plasma and are useful tools to deduce plasma parameters difficult to measure directly, see e.g. Nakariakov & Verwichte (2005); Van Doorsselaere et al. (2011); Nakariakov et al. (2016); Van Doorsselaere et al. (2016b); Nakariakov & Kolotkov (2020); Kupriyanova et al. (2020). The fast sausage mode is an essentially axisymmetric compressive mode where the magnetic field and the density perturbations are almost perpendicular and the plasma motion is mainly perpen-

dicular to the unperturbed loop axis. Due to the expected short periods of the mode (of a few seconds), instruments of high time resolution observing at microwave and hard X-ray wavelengths are required (Melnikov et al. 2005; Inglis et al. 2008). Particularly, the first fundamental (global trapped) sausage mode observation, with a peak at 17s, was detected by Nakariakov et al. (2003) using the Nobeyama Radioheliograph at 17 GHz and 34 GHz.

Observations show that QPP that are detected in the microwave and X-ray bands, have much deeper modulations depths than EUV-visible-light-MHD waves (sometimes up to a hundred percent). Thus, it is important to provide a criterion to establish if the nature of these two types of oscillations are of the same nature (Nakariakov et al. 2006; Kupriyanova et al. 2020).

Mossessian & Fleishman (2012); Reznikova et al. (2014); Kuznetsov et al. (2015) modelled the modulation depth (hereafter MD) of the gyrosynchotron (GS) emission by MHD oscillations using a specific geometrical perturbation of a given monochromatic frequency and usual flaring parameters. In particular, Reznikova et al. (2014, hereafter R14) found that the resulting MD of fast sausage modes is spatially dependent on the inhomogeneity of its oscillating source, i.e., depending on the viewing angle; and the spatial resolution of the model used for the analysis.

More recently, Capettini et al. (2020, hereafter C20) analysed the capability of different types of perturbations associated with energy fluctuations of the solar corona to excite slow and fast sausage modes in solar flaring loops. In flaring regions, the characteristic conductive heating time is much smaller than the radiative cooling one. Thus, typical impulsive disturbance are capable of impulsively modify the entire internal temperature of the loop exciting a dominant fast sausage mode.

In this paper the aim is to analyse the R14 results – specifically the importance of the viewing angle, the spatial resolution (a part of the loop or the entire loop) and the frequency variations in the MD of the GS emission– considering the chromosphere and using a global impulsive perturbation of overlapping frequencies with the capability to excite a sausage mode as found in C20. The purpose is to investigate if the R14 results obtained by a linear and monochromatic analysis are also valid when perturbing in a more natural context, i.e., with a more general perturbation of energy, of the order of a microflare energy. Also, to consider different spatial resolutions is of interest to analyse the oscillatory features that could remain when the loop radiation is integrated as a whole in order to compare with different observing frames, e.g., the QPP description in a point-like stellar flaring loop.

In Section 2 we detail the model used to simulate the sausage mode oscillations and the tools to emulate its GS emission. Results are shown in Section 3. Through a wavelet analysis on the density and the intensity parameters we study the dominant mode developed considering both a small central region of the loop and the entire loop. Also, in this section we show the GS intensity and its relation with the magnetic field and the density. We also analyse the behaviour of the MD when the frequencies and the LOS viewing angles are changed. Finally, in Section 4 we present the main conclusions.

2. Model

We solve the 2.5D ideal magnetohydrodynamic (MHD) equations to study the sausage oscillations of coronal loops based on the model proposed by C20. **Considering a straight coronal loop of typical flaring parameters in equilibrium with its surrounding medium (corona and chromosphere), we set the C20 geometrical dimensions (length $L = 25$Mm and width $w = 6$Mm). We perturb the initial equilibrium configuration with a global energy deposition, that is, we instantaneously increase the temperature along the entire loop. This type of perturbation occurs in flaring regions where the conductive heating times are very small. In this scenario an additional heat applied to one end of the loop immediately heats up the entire loop.** To analyse how this perturbation is able to produce GS emission, we choose as reference conditions the "Base model" initial plasma parameters of R14 (see the Corona and Loop columns of Table 1).

We excite the initial states instantaneously increasing the temperature of the reference loop: $\Delta T = (1, 3, 10, 20)$ MK and we name each disturbed case as B1, B3, B10, and B20, respectively (see last four columns of Table 1). Each increment resembles the action of a microflare and is equivalent to an increment in the internal energy $\Delta E_i = \frac{nk\Delta T}{\gamma-1}V = (1.45\ 10^{27}, 4.37\ 10^{27}, 1.45\ 10^{28}, 2.91\ 10^{28})$ **erg, respectively, and where V is the volume of the cylinder**. The β-parameters, the sound and Alfvén speeds are also shown in the Table.

2.1. Radio emission

We analyse the sausage radio emission in different scenarios treating the numerical data with the FoMo-GS tool (Van Doorsselaere et al. 2016a). **To describe the non-thermal electron distribution, we consider a distribution function $G(E, \mu) = u(E)g(\mu)$ where $u(E)$ is the energy and $g(\mu)$ is the angular distribution functions, respectively (Fleishman & Kuznetsov 2010; Kuznetsov & Fleishman 2021). We taking to account two electron distributions. A single power-law distribution with $u(E) = a\ E^{-\delta}$ for $E_{min} < E < E_{max}$, where the electron spectral index $\delta = 3.5$, $E_{min} = 0.1$ MeV, and $E_{max} = 10$ MeV. A non-zero non-thermal electron number density is used inside the loop: $n_{n-t} = n/200$. For the double power-law distribution, we choose $\delta = 1.5$ for $E_{min} < E \leq E_{break}$, and $\delta = 3$ for $E_{break} \leq E < E_{max}$, where $E_{min} = 0.01$ MeV, $E_{break} = 0.5$ MeV, and $E_{max} = 10$ MeV. For this distribution, the non-thermal electron number density inside the loop is $n_{n-t} = n/4000$. The distribution over the pitch angle is isotropic with $g(\mu) = 0.5$.**

Given the axisymmetry of the problem, to calculate the GS emission of a cylindrical coronal loop, we have to construct 3 dimensional data from the 2.5D numerical result. Thus, we perform a revolution of the 2.5D data around the loop axis. We consider two cases: 1) the integration along the line of sight (LOS) of a central pixel of 0.″5 (equivalent to 5×5 simulation cells around (1, 17.5) Mm, hereafter "**Central pixel**", shown in Fig. 1) and 2) the integration of the whole loop, to resemble the signal obtained from distant point-like stars (hereafter "**Entire loop**"). Our results do not show significant differences between the single and the double power-law distribution of non-thermal electrons (Shi et al. 2022). We here show the results of the double-law spectrum parameters of R14.

3. Results

3.1. Wavelet analysis

To analyse the modes excited by the global impulsive perturbation in a loop initially in equilibrium, we wavelet analysed the density of detrended data. We found that all cases present the same behaviour, except the amplitude of the Fourier power spectrum which increases an order of magnitude with the increase of

	Corona	Loop	B1	B3	B10	B20
n [cm^{-3}]	2 10^8	10^{10}	10^{10}	10^{10}	10^{10}	10^{10}
T [MK]	2	10	11	13	20	30
B_z [G]	56	53	53	53	53	53
β	0.0004	0.13	0.14	0.17	0.26	0.37
ΔE_i [10^{27}erg]			1.45	4.37	14.5	29.1
c_s [km/s]	210	470	500	540	670	940
v_A [km/s]	11000	1470	1470	1470	1470	1470

Table 1: System initial values for the different simulated cases.

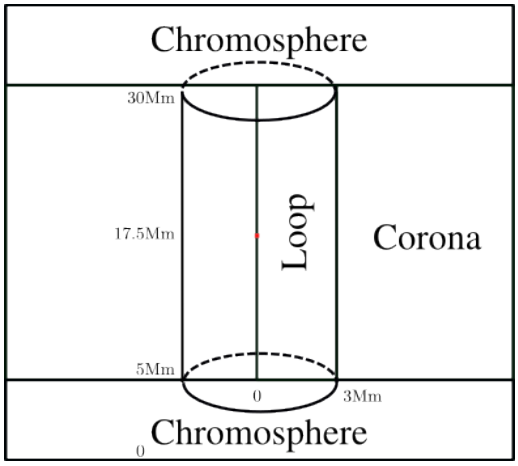

Fig. 1: Scheme of the loop and its environment. The small red point represents a pixel of 0.″5.

the internal energy deposition. Figure 2 shows the wavelet analysis of the B20 case (the other cases's behaviours are similar and are not shown here). In panel (a) we show the density along time, measured at **Central pixel**. In panel (b) we see the wavelet power spectrum of the density during 200 s. In panel (c) we see the Fourier power spectrum. A dominant period of $\sim$ 7 s corresponding to a fast sausage mode ($\tau \sim 2w/v_A$) with an amplitude significantly high during 170 s is obtained. A $\sim$ 32 s period of a slow mode ($\tau \sim L/c_s$) is also found, which is not significant.

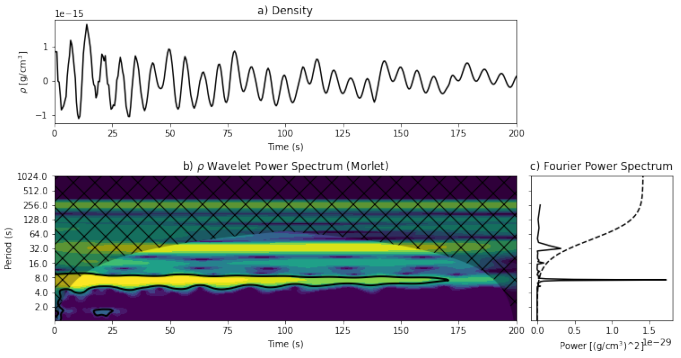

Fig. 2: (a) Density along time measured at **Central pixel** of the B20 case. (b) Wavelet power spectrum of the density along 200 s. The black cross-lines show the part of the spectrum that is inside the cone of influence. The dominant period of $\sim$ 7 s is enclosed by the black contours of 99% confidence level. (c) Fourier power spectrum (solid line) and the 99% confidence spectrum (dashed line).

The Razin suppression (Razin 1960a, 1960b)[1] is negligible at frequencies larger than 1 GHz, thus we analyse the cases at frequencies larger than 10 GHz. We estimate the radiation emitted by the **Central pixel** and we calculate the GS emission at different frequencies (10 GHz and 100 GHz) for all cases. We only show here the B20 case (100 GHz) due to the similar behaviour between the different frequencies except for the magnitude of the Fourier power spectrum. From Fig. 3, we note that the fast sausage mode is the main mode observed. Also, a first harmonic of 3 s has appeared, while the previous slow mode has disappeared. The sausage first harmonic corresponds to a higher frequency oscillation observed in the first 25 s.

We see from Fig. 4 that similar results are obtained if we consider the **Entire loop**. The higher frequencies appearing in Fig. 3 (see e.g. panel (a)) in the first 25 s are now nearly invisible due to the average performed.

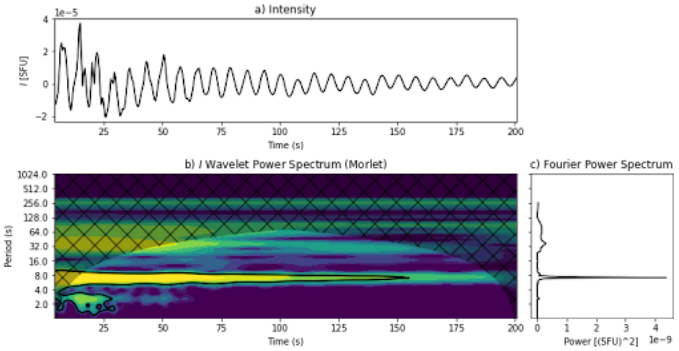

Fig. 3: (a) Intensity along time measured at the **Central pixel** for B20 case, at 100 GHz. Panels (b) and (c) describe the same features as in Fig. 2.

3.2. Imaging analysis

We analyse the emission intensity by processing the numerical data (Fig. 5), integrating the radiation along the LOS at the angle 30° **and** 85° and frequency 100 GHz, for the B20 case at 10 s. **Note that when the LOS angle is smaller, the path length of the emission integration is larger and the intensity increases significantly, by at least an order of magnitude, when the angle varies from** 85° **to** 30°**. The path length that comes from smaller angles necessarily crosses zones of maximum and minimum GS emission, therefore it is reasonable that the integrated emission obtained never reaches its minimum value as it does when the angle is transversal to the loop. Also, a smooth modulation of the intensity which mainly responds**

[1] As the Razin effect states, the GS radiation is suppressed at frequencies where the refractive index becomes significantly less than unity.

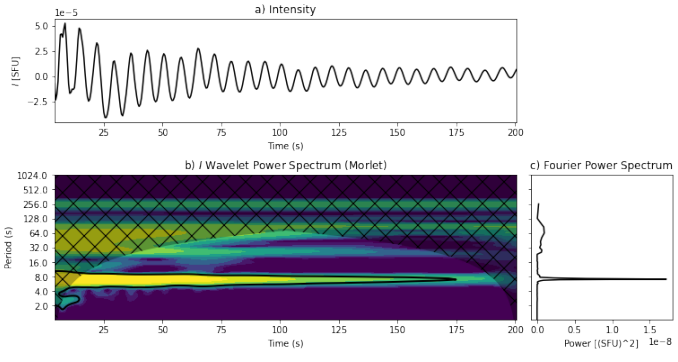

Fig. 4: Same as Fig. 3 for the **Entire loop**.

to the density and the magnetic field pattern (see Fig. 6) is observed. The lower intensity along the loop axis is related with the larger optical depth i.e., the integrated path is larger at the axis location.

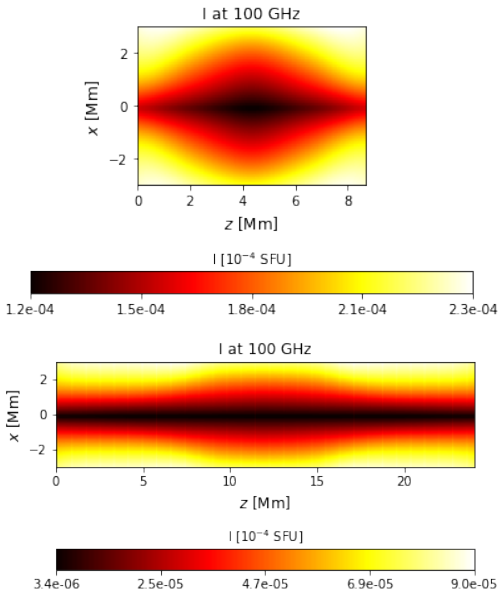

Fig. 5: **Intensity obtained by integrating the radiation along the LOS angle of** 30° **(upper panel) and** 85° **(lower panel) at frequency** 100 **GHz, for case B20 at** $t = 10$ **s.**

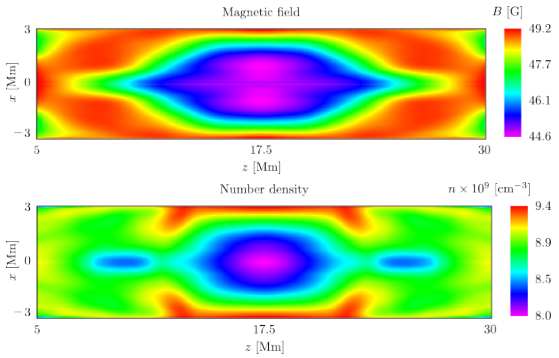

Fig. 6: Magnetic field and number density at $t = 10$ s for B20.

3.3. Radio frequencies analysis

The left panel of Fig. 7 shows the MD ($\delta I/I_0 = (I_\nu(t) - I_\nu(0))/I_\nu(0)$, where $I_\nu(t)$ is the time series of the intensity at the selected frequency ν) for two oscillation periods for radio frequencies 10 GHz (blue line), 35 GHz (orange line) and 100 GHz (green line), respectively and for B20 case, considering the **Central pixel** integration. When the loop is observed at 85° we find slightly larger MDs with the increase of the frequency[2]. The same occurs for the sequence of frequencies at angles 30°, 45° and 60° (not shown here). This trend does not occur in R14 for certain angles e.g. 30° and 45°. This is due to a particular pattern associated with the larger radio frequencies. The higher the frequency, the smaller the amplitude of the oscillating intensity. However, as the intensity values are very small for large frequencies ($I \propto \nu^{1.22-0.9\delta}$) the denominator is small enough to produce a significant increase in the MD value. This pattern is also present in the **Entire loop** integration, with a smaller contrast due to the average performed. For both the **Central pixel** and the **Entire loop** integration, we see on the right panels of Fig. 7 and 8, respectively, that larger initial energy perturbations imply larger MDs. The blue, orange, green and red lines represent the B1, B3, B10 and B20 cases, respectively.

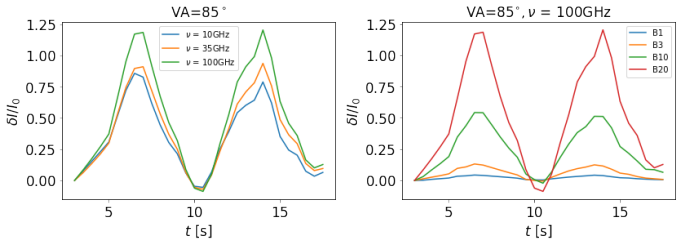

Fig. 7: Left panel: MD measured along the **Central pixel** for B20 case at different frequencies. Right panel: Changes of MD through different cases calculated at 100 GHz; both panels with a viewing angle of 85°.

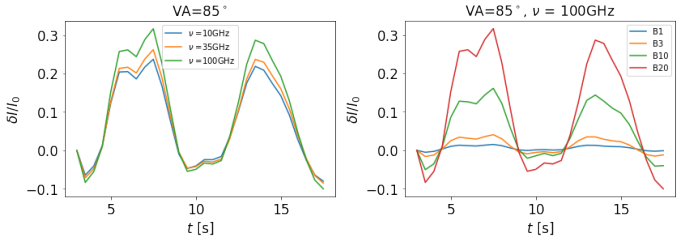

Fig. 8: Same as Fig. 7 for the **Entire loop**.

3.4. Viewing angles analysis

Concerning different angles, we analyse the temporal MD for the **Central pixel** integration (left panel of Fig. 9), considering 30° (red line), 45° (green line), 60° (orange line) and 85° (blue line) viewing angles for the B20 case. Smaller MDs are obtained for smaller angles at 100 GHz (in the average the 30° case is smaller in a 43% than 85°). Considering the **Entire loop** integration, the MD is smaller than in the **Central pixel** integration due to the average performed. However, the correlation between the MD and

[2] The trend is not changed when the pixel location is changed.

the variation of the LOS angle is opposite, i.e., the MD increases when the angle decreases (in the average the 30° case is larger in a 13% than the 85° case) (see right panel of the figure). **From Fig. 10, we note as the angle is increased, for the Entire loop, the average over the whole loop produces a flatter modulation in intensity, resulting in a smaller MD.** Unlike R14, both the **Central pixel** integration and the **Entire loop** integration do not present relative phase changes, and the same occurs for the other frequencies (10 GHz and 35 GHz), not shown here.

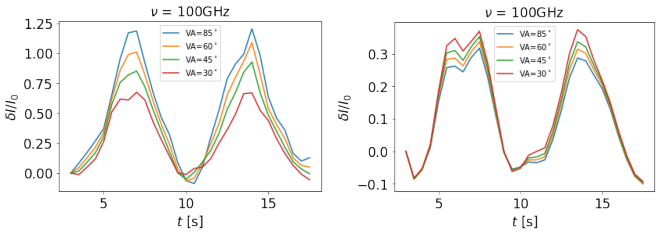

Fig. 9: Left panel: MD of the **Central pixel** integration for the B20 case at different angles. Right panel: same as left panel for the **Entire loop** integration.

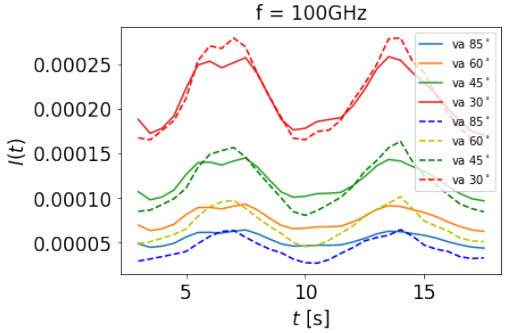

Fig. 10: Intensity of the **Central pixel** (dashed line) and **Entire loop** (solid line) integration for the B20 case at different angles.

3.5. Mean modulation depth

To quantify the intensity deviation from its average value we define the mean modulation depth (MMD) as $\Delta = 2 \max\left(\frac{I(t)-\langle I\rangle}{\langle I\rangle}\right)$, where $\langle I\rangle$ is the intensity average over a period.

In Fig. 11 we show the results found for the **Central pixel** integration. The left and middle panels show a clear trend of the increase in the MMD curve as the frequency and the viewing angle increase, respectively. Note that only the B20 case, with the larger viewing angle, reaches almost 100% of the modulation depth, for the highest frequency. As Kupriyanova et al. (2016) we found that our perturbations have finite amplitudes. Thus, the perturbations could excite sausage modes with finite amplitudes as well, justifying the deep MMD observed. This implies that we can use the high modulation depth cases as seismological tools to detect strong magnetic field cases.

We also compare the increment of the MMD with the increment of the energy deposition, i.e. cases B1, B3, B10 and B20 have an increment of $f_E = \Delta E_i/E_{i,\mathrm{eq}} = (1.1, 1.3, 2, 3)$ with respect to the equilibrium value, respectively. Thus, we calculate the ratio between the MMD and the linear increment of the energy deposition centred at 0 (to have a common origin for comparison), i.e. $\Delta/(f_E - 1)$. From Fig. 11 we note that, for all frequencies, the increase in MMD is not linear with the energy deposition increment. In fact, we note a saturation of the MMD increment with the energy deposition.

We perform the same analysis for the **Entire loop** (Fig. 12). As a difference with the **Central pixel** case the left panel clearly shows that, for a given frequency, the MMD increases when the viewing angles decrease. The middle and right panel show similar results as the **Central pixel** case but with smaller values.

4. Conclusions

Via 2.5D numerical simulations, and impulsively perturbing a straight loop system (length of 25 Mm, and width of 6 Mm) of coronal parameters in equilibrium with its environment (chromosphere and corona), we analysed the excitation of dominant fast sausage modes. A wavelet analysis performed over the GS radiation emission of a **Central pixel** showed that, for all the energy perturbations used, a fast fundamental sausage mode of $\sim$ 7 s developed during $\sim$ 170 s. Also, we found a first harmonic of the fast sausage mode of 3 s lasting for $\sim$ 25 s, and a weak slow sausage mode, below a wavelet confidence level. The general behaviour of the radiation intensity obtained from the wavelet analysis resembles the observational description shown in Kupriyanova et al. (2020) (see figure 5 of these authors), where the presence of a fast mode, with its first harmonic together with a similar decay pattern, suggests a common explanation of the phenomenon.

Our work shows that most of the results obtained by R14, where the excitation of the sausage mode was performed by a forced, monochromatic and linear perturbation, remain when an impulsive excitation of the mode takes place, i.e., when a typical fluctuation of the plasma parameters is able to impulsively trigger the oscillation and its corresponding GS emission. As in R14, the increase of radio brightness corresponds to the areas of stronger magnetic field strength and higher density for all frequencies. Also, we found that for a **Central pixel** integration, the larger the radio frequency and the larger the LOS angle, with respect to the loop axis, the larger the MD obtained.

We also considered the integration of the intensity over the **Entire loop**. As in the **Central pixel** integration we found that the larger the frequency, the larger the MD obtained. However, we here found that the larger the LOS angle, with respect to the loop axis, the smaller the MD obtained. This should be a difference between high resolution observations of sausage modes, as in solar loops, and measurement of sausage modes in low resolution, as in stellar flares observations. Thus, this eventually provides a tool to distinguish between sausage modes and other sources of QPP signals.

On the other hand, the increase of the energy deposition implies, for both spatial resolutions, an increase of the MD. For the **Central pixel** resolution and for the lower energy B1 case, considering 100GHz, the MD is $\sim$ 104%, for B3 is $\sim$ 113%, for B10 is $\sim$ 154% and for B20 is $\sim$ 220%, with respect to their initial values, respectively. This could show that fast MHD modes triggered by impulsive energy depositions of the order of a microflare energy are able to reproduce deep MDs in radio emission as occur in solar observations. When considering the low resolution integration (the **Entire loop** integration) the increase of the MD is at the most of 132% in the more energetic case of B20. The MD provides information on the deviation of intensity from its initial value, while the MMD describes the deviation of intensity from its mean value. This is important for the interpretation of observations. The MMD results show the same trends as the MD results. Also, in both cases, **Central pixel** and **Entire loop**,

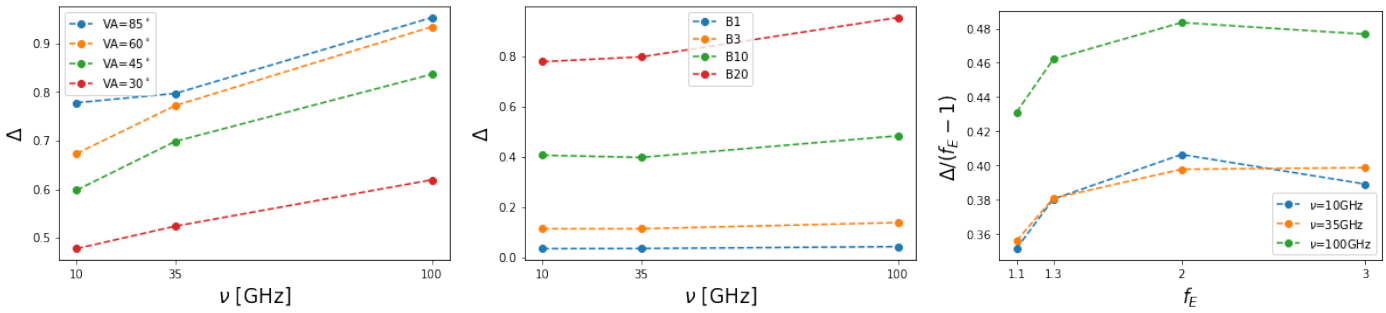

Fig. 11: **Central pixel**. Left panel: MMD with frequency for case B20 at different viewing angles. Middle panel: Same as left panel for viewing angle 85° at different cases. Right panel: Ratio between MMD and linear growth of energy deposition.

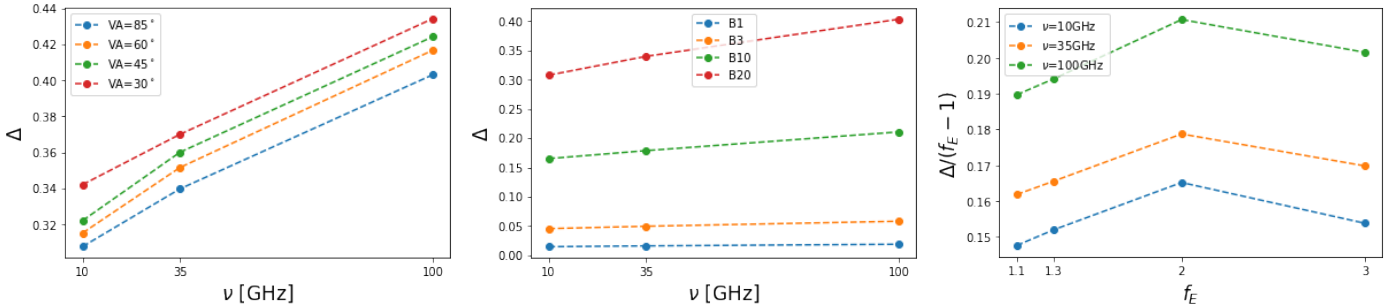

Fig. 12: Same as Fig. 11 for **Entire loop**.

we found that the increment of the MMD is not linear with the increment of the energy deposition.

We schematically summarise our results as: 1) We confirm that, for all spatial resolutions, the larger the GS frequency of sausage modes, the larger the MD and MMD; 2) Depending on the high and low spatial resolution of the integration, larger LOS angles give rise to larger MDs and MMDs and smaller MDs and MMDs, respectively; 3) We show that large MDs and MMD are also associated with sausage modes when they are obtained considering more general contexts and perturbations; 4) The regularities found here suggest a way of differentiating sausage mode QPPs from QPPs of other origin; 5) These results would also allow to identify sausage mode signals in stellar flares.

Acknowledgements. MC and AC are members of the Carrera del Investigador Científico (CONICET). MC and AC acknowledge support from SECYT-UNC grant number PC No. 33620180101147CB and from PIP under grant number No. 11220200103150CO. TVD was supported by the European Research Council (ERC) under the European Union's Horizon 2020 research and innovation programme (grant agreement No 724326), the C1 grant TRACEspace of Internal Funds KU Leuven, and a Senior Research Project (G088021N) of the FWO Vlaanderen. Also, we thank the Centro de Cómputo de Alto Desempeño (UNC), where the simulations were carried out. This research was supported by the International Space Science Institute (ISSI) in Bern, through ISSI International Team project N° 527 Bridging New X-ray Observations and Advanced Models of Flare Variability: A Key to Understanding the Fundamentals of Flare Energy Release.

References

Capettini, H., Cécere, M., Costa, A., Krause, G., & Reula, O. 2020, A&A, 644, A106
Carrington, R. C. 1859, MNRAS, 20, 13
Cho, I. H., Cho, K. S., Nakariakov, V. M., Kim, S., & Kumar, P. 2016, ApJ, 830, 110
Fleishman, G. D. & Kuznetsov, A. A. 2010, ApJ, 721, 1127
Inglis, A. R., Nakariakov, V. M., & Melnikov, V. F. 2008, A&A, 487, 1147
Kolotkov, D. Y., Nakariakov, V. M., Holt, R., & Kuznetsov, A. A. 2021, ApJ, 923, L33
Kupriyanova, E., Kolotkov, D., Nakariakov, V., & Kaufman, A. 2020, Solar-Terrestrial Physics, 6, 3
Kupriyanova, E. G., Kashapova, L. K., Reid, H. A. S., & Myagkova, I. N. 2016, Sol. Phys., 291, 3427
Kuznetsov, A. A. & Fleishman, G. D. 2021, ApJ, 922, 103
Kuznetsov, A. A., Van Doorsselaere, T., & Reznikova, V. E. 2015, Sol. Phys., 290, 1173
McLaughlin, J. A., Nakariakov, V. M., Dominique, M., Jelínek, P., & Takasao, S. 2018, Space Sci. Rev., 214, 45
Melnikov, V. F., Reznikova, V. E., Shibasaki, K., & Nakariakov, V. M. 2005, A&A, 439, 727
Mossessian, G. & Fleishman, G. D. 2012, ApJ, 748, 140
Nakariakov, V. M., Foullon, C., Verwichte, E., & Young, N. P. 2006, A&A, 452, 343
Nakariakov, V. M. & Kolotkov, D. Y. 2020, ARA&A, 58, 441
Nakariakov, V. M., Kolotkov, D. Y., Kupriyanova, E. G., et al. 2019, Plasma Physics and Controlled Fusion, 61, 014024
Nakariakov, V. M., Melnikov, V. F., & Reznikova, V. E. 2003, A&A, 412, L7
Nakariakov, V. M., Pascoe, D. J., Sych, R., & van Driel-Gesztelyi, L. 2016, Sol. Phys., 291, 3139
Nakariakov, V. M. & Verwichte, E. 2005, Living Reviews in Solar Physics, 2, 3
Reznikova, V. E., Antolin, P., & Van Doorsselaere, T. 2014, ApJ, 785, 86
Shi, M., Li, B., & Guo, M. 2022, ApJ, 937, L25
Van Doorsselaere, T., Antolin, P., Yuan, D., Reznikova, V., & Magyar, N. 2016a, Frontiers in Astronomy and Space Sciences, 3, 4
Van Doorsselaere, T., De Groof, A., Zender, J., Berghmans, D., & Goossens, M. 2011, ApJ, 740, 90
Van Doorsselaere, T., Kupriyanova, E. G., & Yuan, D. 2016b, Sol. Phys., 291, 3143
Zimovets, I. V., McLaughlin, J. A., Srivastava, A. K., et al. 2021, Space Sci. Rev., 217, 66